

Polyp-PVT: Polyp Segmentation with Pyramid Vision Transformers

Bo Dong, Wenhai Wang, Deng-Ping Fan, Jinpeng Li, Huazhu Fu, and Ling Shao

Abstract—Most polyp segmentation methods use CNNs as their backbone, leading to two key issues when exchanging information between the encoder and decoder: 1) taking into account the differences in contribution between different-level features and 2) designing an effective mechanism for fusing these features. Unlike existing CNN-based methods, we adopt a transformer encoder, which learns more powerful and robust representations. In addition, considering the image acquisition influence and elusive properties of polyps, we introduce three standard modules, including a cascaded fusion module (CFM), a camouflage identification module (CIM), and a similarity aggregation module (SAM). Among these, the CFM is used to collect the semantic and location information of polyps from high-level features; the CIM is applied to capture polyp information disguised in low-level features, and the SAM extends the pixel features of the polyp area with high-level semantic position information to the entire polyp area, thereby effectively fusing cross-level features. The proposed model, named Polyp-PVT, effectively suppresses noises in the features and significantly improves their expressive capabilities. Extensive experiments on five widely adopted datasets show that the proposed model is more robust to various challenging situations (e.g., appearance changes, small objects, rotation) than existing representative methods. The proposed model is available at <https://github.com/DengPingFan/Polyp-PVT>.

Index Terms—Polyp segmentation, pyramid vision transformer, colonoscopy, computer vision

I. INTRODUCTION

Colonoscopy is the gold standard for detecting colorectal lesions since it enables colorectal polyps to be identified and removed in time, thereby preventing further spread. As a fundamental task in medical image analysis, polyp segmentation (PS) aims to locate polyps accurately in the early stage, which is of great significance in the clinical prevention of rectal cancer. Traditional PS models mainly rely on low-level features, e.g., texture [1], geometric features [2], simple linear iterative clustering superpixels [3]. However, these methods yield low-quality results and suffer from poor generalization ability. With the development of deep learning, PS has achieved promising progress. In particular, the U-shaped [4] has attracted significant attention due to its ability to adopt multi-level features for reconstructing high-resolution results.

B. Dong and D.-P. Fan are with the Nankai University, Tianjin, 300350, China. * Corresponding author (dengpfan@gmail.com).

W. Wang is with Shanghai Artificial Intelligence Laboratory, Shanghai, 200232, China

J. Li is with Computer Vision Lab, Inception Institute of Artificial Intelligence, Abu Dhabi 00000, UAE

H. Fu is with Institute of High Performance Computing, Agency for Science, Technology and Research, Singapore 138632, Singapore

L. Shao is with UCAS-Terminus AI Lab, Terminus Group, Chongqing 400042, China

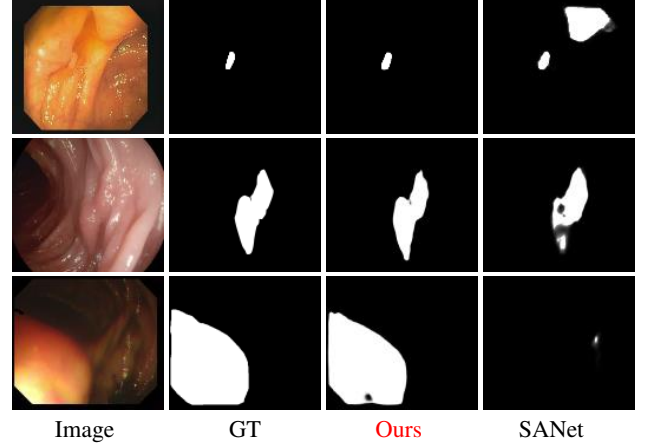


Fig. 1. The segmentation examples of our model and SAnet [7] with different challenge cases, e.g., camouflage (1st and 2nd rows) and image acquisition influence (3rd row). The images from top to bottom are from ClinicDB [8], ETIS [9], and ColonDB [10], which show that our model has better generalization ability.

PraNet [5] employs a two-stage segmentation approach, adopting a parallel decoder to predict rough regions and an attention mechanism to restore a polyp’s edges and internal structure for fine-grained segmentation. ThresholdNet [6] is a confidence-guided data enhancement method based on a hybrid manifold for solving the problems caused by limited annotated data and imbalanced data distributions.

Although these methods have greatly improved accuracy and generalization ability compared to traditional methods, it is still challenging for them to locate the boundaries of polyps, as shown in Fig. 1, for several reasons: (1) **Image noise**. During the data collection process, the lens rotates in the intestine to obtain polyp images from different angles, which also causes motion blur and reflector problems. As a result, this greatly increases the difficulty of polyp detection; (2) **Camouflage**. The color and texture of polyps are very similar to surrounding tissues, with low contrast, providing them with powerful camouflage properties [11], [12], and making them difficult to identify; (3) **Polycentric data**. Current models struggle to generalize to multicenter (or unseen) data with different domains/distributions. To address the above issues, our contributions in this paper are as follows:

- We present a novel polyp segmentation framework, termed Polyp-PVT. Unlike existing CNN-based methods, we adopt the pyramid vision transformer as an encoder to extract more robust features.
- To support our framework, we introduce three simple modules. Specifically, the cascaded fusion module (CFM)

collects polyps' semantic and location information from the high-level features through progressive integration. Meanwhile, the camouflage identification module (CIM) is applied to capture polyp cues disguised in low-level features, using an attention mechanism to pay more attention to potential polyps, reducing incorrect information in the lower features. We further introduce the similarity aggregation module (SAM) equipped with a non-local and convolutional graph layer to mine local pixels and global semantic cues from the polyp area.

- Finally, we conduct extensive experiments on five challenging benchmark datasets, including Kvasir-SEG [13], ClinicDB [8], ColonDB [10], Endoscene [14], and ETIS [9], to evaluate the performance of the proposed Polyp-PVT. On ColonDB, our method achieves a mean Dice (mDic) of 0.808, which is 5.5% higher than the existing cutting-edge method SANet [7]. On the ETIS dataset, our model achieves a mean Dice (mDic) of 0.787, which is 3.7% higher than SANet [7].

II. RELATED WORKS

A. Polyp Segmentation

Traditional Methods. Computer-aided detection is an effective alternative to manual detection, and a detailed survey has been conducted on detecting ulcers, polyps, and tumors in wireless capsule endoscopy imaging [15]. Early solutions for polyp segmentation were mainly based on low-level features, such as texture [2], geometric features [2], or simple linear iterative clustering superpixels [3]. However, these methods have a high risk of missed or false detection due to the high similarity between polyps and surrounding tissues.

Deep Learning-Based Methods. Deep learning techniques [16]–[25] have greatly promoted the development of polyp segmentation tasks. Akbari *et al.* [26] proposed a polyp segmentation model using a fully convolutional neural network, whose segmentation results are significantly better than traditional solutions. Brandao *et al.* [27] used the shape from the shading strategy to restore depth, merging the result into an RGB model to provide richer feature representations. More recently, encoder-decoder-based models, such as U-Net [4], UNet++ [28], and ResUNet++ [29], have gradually come to dominate the field with excellent performance. Sun *et al.* [30] introduced a dilated convolution to extract and aggregate high-level semantic features with resolution retention to improve the encoder network. Psi-Net [31] introduced a multi-task segmentation model that combines contour and distance map estimation to assist segmentation mask prediction. Hemin *et al.* [32] first attempted to use a deeper feature extractor to perform polyp segmentation based on Mask R-CNN [33].

Different from the methods based on U-Net [4], [28], [34], PraNet [5] uses reverse attention modules to mine boundary information with a global feature map, which is generated by a parallel partial decoder from high-level features. Polyp-Net [35] proposed a dual-tree wavelet pooling CNN with a local gradient-weighted embedding level set, effectively avoiding erroneous information in high signal areas, thereby significantly reducing the false positive rate. Rahim *et al.* [36]

proposed to use different convolution kernels for the same hidden layer for deeper feature extraction with MISH and rectified linear unit activation functions for deep feature propagation and smooth non-monotonicity. In addition, they adopted joint generalized intersections, which overcome scale invariance, rotation, and shape differences. Jha *et al.* [37] designed a real-time polyp segmentation method called ColonSNet. For the first time, Ahmed *et al.* [38] applied the generative adversarial network to the field of polyp segmentation. Another interesting idea proposed by Thambawita *et al.* [39] is introducing pyramid-based augmentation into the polyp segmentation task. Further, Tomar *et al.* [40] designed a dual decoder attention network based on ResUNet++ for polyp segmentation. More recently, MSEG [41] improved the PraNet and proposed a simple encoder-decoder structure. Specifically, they used Hardnet [42] to replace the original backbone network Res2Net50 backbone network and removed the attention mechanism to achieve faster and more accurate polyp segmentation. As an early attempt, Transfuse [43] was the first to employ a two-branch architecture combining CNNs and transformers in a parallel style. DCRNet [44] uses external and internal context relations modules to separately estimate the similarity between each location and all other locations in the same and different images. MSNet [45] introduced a multi-scale subtraction network to eliminate redundancy and complementary information between the multi-scale features. Providing a comprehensive review of polyp segmentation is beyond the scope of this paper. In Tab. I, however, we briefly survey representative works related to ours.

B. Vision Transformer

Transformers use multi-head self-attention (MHSA) layers to model long-term dependencies. Unlike the convolutional layer, the MHSA layer has dynamic weights and a global receptive field, making it more flexible and effective. The transformer [65] was first proposed by Vaswani *et al.* for the machine translation task and has since extensively influenced the natural language processing field. To apply transformers to computer vision tasks, Dosovitskiy *et al.* [66] proposed a vision transformer (ViT), which was the first pure transformer for image classification. ViT divides an image into multiple patches, which are sequentially sent to a transformer encoder after being encoded, and then an MLP is used to perform image classification. HVT [67] is based on a hierarchical progressive pooling method to compress the sequence length of a token and reduce the redundancy and number of calculations in ViT. The pooling-based vision transformer [68] draws on the principle of CNNs whereby, as the depth increases, the number of feature map channels increases, and the spatial dimension decreases. Yuan *et al.* [69] pointed out that the simple token structure in ViT cannot capture important local features, such as edges and lines, which reduces the training efficiency and leads to redundant attention mechanisms. T2T ViT was thus proposed to use layer-by-layer tokens-to-token transformation to gradually merge neighboring tokens and model local features while reducing the token's length. TNT [70] employs a transformer suitable for fine-grained image tasks, which

TABLE I

A SURVEY ON POLYP SEGMENTATION. CL = CVC-CLINIC, EL = ETIS-LARIB, C6 = CVC-612, AM = ASU-MAYO [46], [47], ES = ENDOSCENE, DB = COLONDB, CV = CVC-VIDEOCLINICDB, C = COLON, ED = ENDOTECT 2020, KS = KVASIR-SEG, KCS = KVASIR CAPSULE-SEG, PRANET = SAME TO DATASETS USED IN PRANET [5], IS = IMAGE SEGMENTATION, VS = VIDEO SEGMENTATION, CF = CLASSIFICATION, OD = OBJECT DETECTION, OWN = PRIVATE DATA. CSCP [1], APD [2], SBCP [3], FCN [26], D-FCN [27], UNET++ [28], PSI-NET [31], MASK R-CNN [32], UDC [30], THRESHOLDNET [6], MI2GAN [48], ACSNet [49], PRANET [5], GAN [38], APS [50], PFA [39], MMT [51], U-NET-RESNET50 [34], SURVEY [15], POLYP-NET [35], DEEP CNN [36], EU-NET [52], DSAS [53], U-NET-MOBILENETV2 [54], DCRNET [44], MSEG [41], FSSNET [55], AG-CUREsNeSt [56], MPAPS [57], RESUNET++ [58], NANONET [59], COLONSEGNET [37], SEGTRAN [60], DDANET [40], UACANET [61], DIVERGENTNET [62], DWHIERASEG [63], TRANSFUSE [43], SANET [7], PNS-NET [64].

No.	Model	Publication	Code	Type	Dataset	Core Components
1	CSCP	IJPRAI	N/A	IS	Own	Adaptive-scale candidate
2	APD	TMI	N/A	IS	Own	Geometrical analysis, binary classifier
3	SBCP	SPMB	N/A	IS	Own	Supersixel
4	FCN	EMBC	N/A	IS	DB	FCN and patch selection
5	D-FCN	JMRR	N/A	IS	CL, EL, AM, and DB	FCN and Shape-from-Shading (SfS)
6	UNET++	DLMIA	PyTorch	IS	AM	Skip pathways and deep supervision
7	Psi-Net	EMBC	PyTorch	IS	Endovis	Shape and boundary aware
8	Mask R-CNN	ISMIC	N/A	IS	C6, EL, and DB	Deep feature extractors
9	UDC	ICMLA	N/A	IS	C6 and EL	Dilation convolution
10	ThresholdNet	TMI	PyTorch	IS	ES and WCE	Learn to threshold Confidence-guided manifold mixup
11	MI2GAN	MICCAI	N/A	IS	C6 and EL	GAN based model
12	ACSNet	MICCAI	PyTorch	IS	ES and KS	Adaptive context selection
13	PraNet	MICCAI	PyTorch	IS	PraNet	Parallel partial decoder attention
14	GAN	MediaEval	N/A	IS	KS	Image-to-image translation
15	APS	MediaEval	N/A	IS	KS	Variants of U-shaped structure
16	PFA	MediaEval	PyTorch	IS	KS	Pyramid focus augmentation
17	MMT	MediaEval	N/A	IS	KS	Competition introduction
18	U-Net-ResNet50	MediaEval	N/A	IS	KS	Variants of U-shaped structure
19	Survey	CMIG	N/A	CF	Own	Classification
20	Polyp-Net	TIM	N/A	IS	DB and CV	Multimodal fusion network
21	Deep CNN	BSPC	N/A	OD	EL	Convolutional neural network
22	EU-Net	CRV	PyTorch	IS	PraNet	Semantic information enhancement
23	DSAS	MIDL	Matlab	IS	KS	Stochastic activation selection
24	U-Net-MobileNetV2	arXiv	N/A	IS	KS	Variants of U-shaped structure
25	DCRNet	ISBI	PyTorch	IS	ES, KS, and PICCOLO	Within-image and cross-image contextual relations
26	MSEG	arXiv	PyTorch	IS	PraNet	Hardnet and partial decoder
27	FSSNet	arXiv	N/A	IS	C6 and KS	Meta-learning
28	AG-CUREsNeSt	RIVF	N/A	IS	PraNet	ResNeSt, attention gates
29	MPAPS	JBHI	PyTorch	IS	DB, KS, and EL	Mutual-prototype adaptation network
30	ResUNet++	JBHI	PyTorch	IS, VS	PraNet and AM	ResUNet++, CRF and TTA
31	NanoNet	CBMS	PyTorch	IS, VS	ED, KS, and KCS	Real-Time polyp segmentation
32	ColonSegNet	Access	PyTorch	IS	KS	Residual block and SENet
33	Segtran	IJCAI	PyTorch	IS	C6 and KS	Transformer
34	DDANet	ICPR	PyTorch	IS	KS	Dual decoder attention network
35	UACANet	ACM MM	PyTorch	IS	PraNet	Uncertainty augmented Context attention network
36	DivergentNet	ISBI	PyTorch	IS	EndoCV 2021	Combine multiple models
37	DWHieraSeg	MIA	PyTorch	IS	ES	Dynamic-weighting
38	Transfuse	MICCAI	PyTorch	IS	PraNet	Transformer and CNN
39	SANet	MICCAI	PyTorch	IS	PraNet	Shallow attention network
40	PNS-Net	MICCAI	PyTorch	VS	C6, KS, ES, and AM	Progressively normalized self-attention network

divides the original image patch and conducts self-attention mechanism calculations in smaller units. Meanwhile, external and internal transformers are used to extract global and local features.

To adapt to dense prediction tasks such as semantic segmentation, several methods [71]–[77] have also introduced the pyramid structure of CNNs to the design of transformer

backbones. For instance, PVT-based models [71], [72] use a hierarchical transformer with four stages, showing that a pure transformer backbone can be as versatile as its CNN counterparts, and performs better in detection and segmentation tasks. In this work, we design a new transformer-based polyp segmentation framework, which can accurately locate the boundaries of polyps even in extreme scenarios.

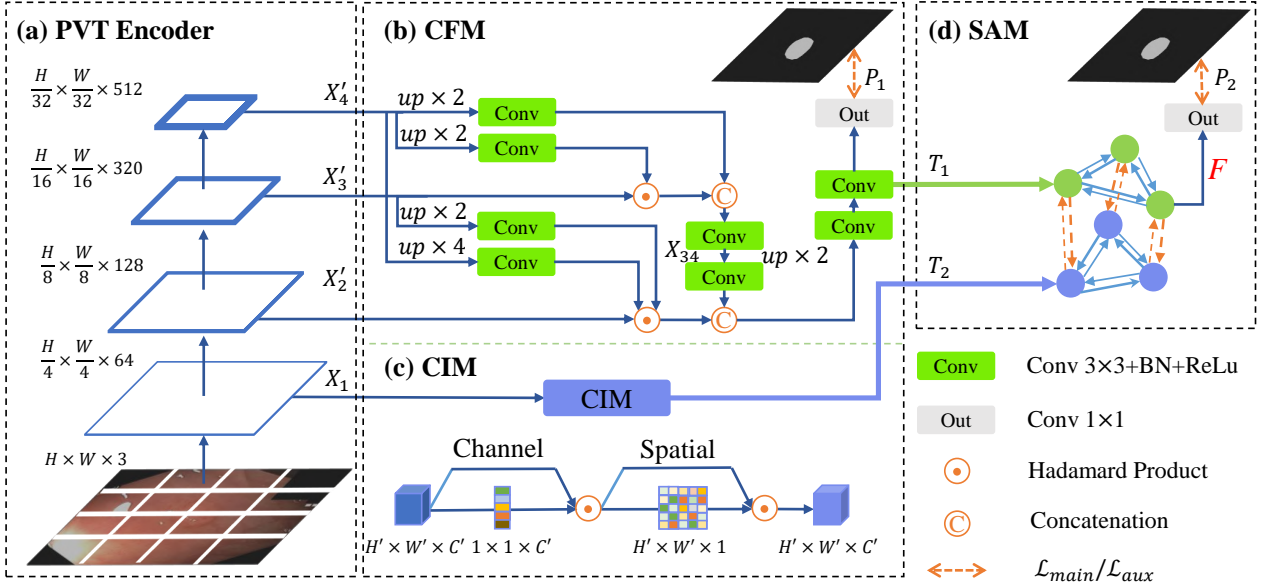


Fig. 2. Framework of our Polyp-PVT, which consists of a pyramid vision transformer (PVT) (a) as the encoder network, (b) cascaded fusion module (CFM) for fusing the high-level feature, (c) camouflage identification module (CIM) to filter out the low-level information, and (d) similarity aggregation module (SAM) for integrating the high- and low-level features for the final output.

III. PROPOSED POLYP-PVT

A. Overall Architecture

As shown in Fig. 2, our Polyp-PVT consists of 4 key modules: namely, a pyramid vision transformer (PVT) encoder, cascaded fusion module (CFM), camouflage identification module (CIM), and similarity aggregation module (SAM). Specifically, the PVT extracts multi-scale long-range dependencies features from the input image. The CFM is employed to collect semantic cues and locate polyps by aggregating high-level features progressively. The CIM is designed to remove noise and enhance low-level representation information of polyps, including texture, color, and edges. The SAM is adopted to fuse the low- and high-level features provided by the CIM and CFM, effectively transmitting the information from the pixel-level polyp to the entire polyp.

Given an input image $I \in \mathbb{R}^{H \times W \times 3}$, we use the transformer-based backbone [71] to extract four pyramid features $X_i \in \mathbb{R}^{\frac{H}{2^{i+1}} \times \frac{W}{2^{i+1}} \times C_i}$, where $C_i \in \{64, 128, 320, 512\}$ and $i \in \{1, 2, 3, 4\}$. Then, we adjust the channel of three high-level features X_2, X_3 and X_4 to 32 through three convolutional units and feed them (i.e., X'_2, X'_3 , and X'_4) to CFM to fuse, leading a feature map $T_1 \in \mathbb{R}^{\frac{H}{8} \times \frac{W}{8} \times 32}$. Meanwhile, low-level features X_1 are converted to $T_2 \in \mathbb{R}^{\frac{H}{4} \times \frac{W}{4} \times 64}$ by the CIM. After that, the T_1 and T_2 are aligned and fused by SAM, yielding the final feature map $F \in \mathbb{R}^{\frac{H}{8} \times \frac{W}{8} \times 32}$. Finally, F is fed into a 1×1 convolutional layer to predict the polyp segmentation result P_2 . We use the sum of P_1 and P_2 as the final prediction. During training, we optimize the model with a main loss $\mathcal{L}_{\text{main}}$ and an auxiliary loss \mathcal{L}_{aux} . The main loss is calculated between the final segmentation result P_2 and the ground truth (GT), which is used to optimize the final polyp segmentation result. Similarly, the auxiliary loss is used to supervise the intermediate result P_1 generated by the CFM.

B. Transformer Encoder

Due to uncontrolled factors in their acquisition, polyp images tend to contain significant noise, such as *motion blur*, *rotation*, and *reflection*. Some recent works [78], [79] have found that the vision transformer [66], [71], [72] demonstrates stronger performance and better robustness to input disturbances than CNNs [16], [17]. Inspired by this, we use a vision transformer as our backbone network to extract more robust and powerful features for polyp segmentation. Different from [66], [73] that uses a fixed ‘‘columnar’’ structure or shifted windowing manner, the PVT [71] is a pyramid architecture whose representation is calculated with spatial-reduction attention operations; thus it enables to reduce the resource consumption. Note that the proposed model is backbone-independent; other famous transformer backbones are feasible in our framework. Specifically, we adopt the PVTv2 [72], which is the improved version of PVT with a more powerful feature extraction ability. To adapt PVTv2 to the polyp segmentation task, we remove the last classification layer and design a polyp segmentation head on top of four multi-scale feature maps (i.e., X_1, X_2, X_3 , and X_4) generated by different stages. Among these feature maps, X_1 gives detailed appearance information of polyps, and X_2, X_3 , and X_4 provide high-level features.

C. Cascaded Fusion Module

To balance the accuracy and computational resources, we follow recent popular practices [5], [80] to implement the cascaded fuse module (CFM). Specifically, we define $\mathcal{F}(\cdot)$ as a convolutional unit composed of a 3×3 convolutional layer with padding set to 1, batch normalization [81] and ReLU [82]. As shown in Fig. 2 (b), the CFM mainly consists of two cascaded parts, as follows:

(1) In part one, we up-sample the highest-level feature map X'_4 to the same size as X'_3 and then pass the result through two convolutional units $\mathcal{F}_1(\cdot)$ and $\mathcal{F}_2(\cdot)$, yieldings: X_4^1 and X_4^2 . Then, we multiply X_4^1 and X_3' and concatenate the result with X_4^2 . Finally, we use a convolution unit $\mathcal{F}_3(\cdot)$ to smooth the concatenated feature, yielding fused feature map $X_{34} \in \mathbb{R}^{\frac{H}{16} \times \frac{W}{16} \times 32}$. The process can be summarized as Eqn. 1.

$$X_{34} = \mathcal{F}_3(\text{Concat}(\mathcal{F}_1(X'_4) \odot X'_3, \mathcal{F}_2(X'_4))), \quad (1)$$

where “ \odot ” denotes the Hadamard product, and $\text{Concat}(\cdot)$ is the concatenation operation along the channel dimension.

(2) As shown Eqn. 2, the second part follows a similar process to part one. Firstly, we up-sample X'_4 , X'_3 , X_{34} to the same size as X'_2 , and smooth them using convolutional units $\mathcal{F}_4(\cdot)$, $\mathcal{F}_5(\cdot)$, and $\mathcal{F}_6(\cdot)$, respectively. Then, we multiply the smoothed X_4 and X_3 with X'_2 , and concatenate the resulting map with up-sampled and smoothed X_{34} . Finally, we feed the concatenated feature map into two convolutional units (*i.e.*, $\mathcal{F}_7(\cdot)$ and $\mathcal{F}_8(\cdot)$) to reduce the dimension, and obtain $T_1 \in \mathbb{R}^{\frac{H}{8} \times \frac{W}{8} \times 32}$, which is also the output of the CFM.

$$T_1 = \mathcal{F}_8(\mathcal{F}_7(\text{Concat}(\mathcal{F}_4(X'_4) \odot \mathcal{F}_5(X'_3) \odot X'_2, \mathcal{F}_6(X_{34})))), \quad (2)$$

D. Camouflage Identification Module

Low-level features often contain rich detail information, such as *texture*, *color*, and *edges*. However, polyps tend to be very similar in appearance to the background. Therefore, we need a powerful extractor to identify the polyp details.

As shown in Fig. 2 (c), we introduce a camouflage identification module (CIM) to capture the details of polyps from different dimensions of the low-level feature map X_1 . Specifically, the CIM consists of a channel attention operation [83] $\text{Att}_c(\cdot)$ and a spatial attention operation [84] $\text{Att}_s(\cdot)$, which can be formulated as:

$$T_2 = \text{Att}_s(\text{Att}_c(X_1)), \quad (3)$$

The channel attention operation $\text{Att}_c(\cdot)$ can be written as follow:

$$\text{Att}_c(x) = \sigma(\mathcal{H}_1(P_{\max}(x)) + \mathcal{H}_2(P_{\text{avg}}(x))) \odot x, \quad (4)$$

where x is the input tensor and $\sigma(\cdot)$ is the Softmax function. $P_{\max}(\cdot)$ and $P_{\text{avg}}(\cdot)$ denote adaptive maximum pooling and adaptive average pooling functions, respectively. $\mathcal{H}_i(\cdot)$, $i \in \{1, 2\}$ shares parameters and consists of a convolutional layer with 1×1 kernel size to reduce the channel dimension 16 times, followed by a ReLU layer and another 1×1 convolutional layer to recover the original channel dimension. The spatial attention operation $\text{Att}_s(\cdot)$ can be formulated as:

$$\text{Att}_s(x) = \sigma(\mathcal{G}(\text{Concat}(R_{\max}(x), R_{\text{avg}}(x)))) \odot x, \quad (5)$$

where $R_{\max}(\cdot)$ and $R_{\text{avg}}(\cdot)$ represent the maximum and average values obtained along the channel dimension, respectively. $\mathcal{G}(\cdot)$ is a 7×7 convolutional layer with padding set to 3.

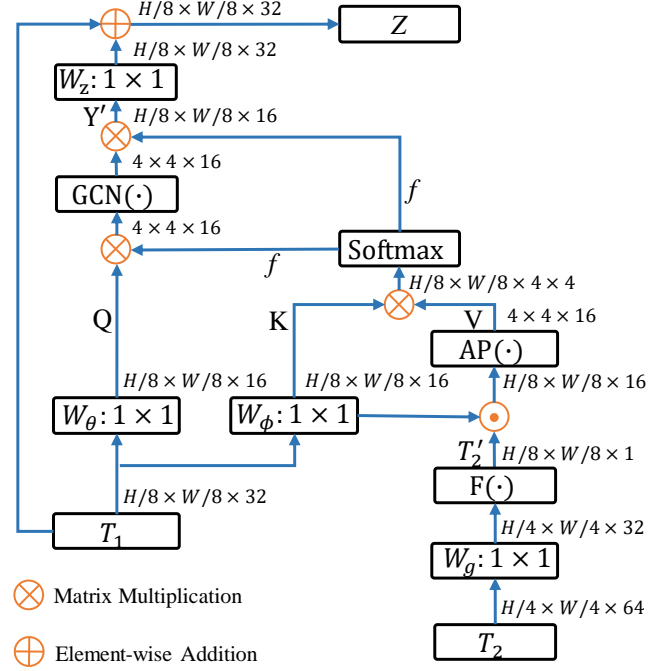


Fig. 3. Details of the introduced SAM. It is composed of GCN and non-local, which extend the pixel features of polyp regions with high-level semantic location cues to the entire region.

E. Similarity Aggregation Module

To explore high-order relations between the lower-level local features from CIM and higher-level cues from CFM. We introduce the non-local [85], [86] operation under graph convolution domain [87] to implement our similarity aggregation module (SAM). As a result, SAM can inject detailed appearance features into high-level semantic features using global attention.

Given the feature map T_1 , which contains high-level semantic information, and T_2 with rich appearance details, we fuse them through self-attention. First, two linear mapping functions $W_\theta(\cdot)$ and $W_\phi(\cdot)$ are applied on T_1 to reduce the dimension and obtain feature maps $Q \in \mathbb{R}^{\frac{H}{8} \times \frac{W}{8} \times 16}$ and $K \in \mathbb{R}^{\frac{H}{8} \times \frac{W}{8} \times 16}$. Here, we take a convolution operation with a kernel size of 1×1 as the linear mapping process. This process can be expressed as follows:

$$Q = W_\theta(T_1), K = W_\phi(T_1). \quad (6)$$

For T_2 , we use a convolutional unit $W_g(\cdot)$ to reduce the channel dimension to 32 and interpolate it to the same size as T_1 . Then, we apply a Softmax function on the channel dimension and choose the second channel as the attention map, leading to $T_2' \in \mathbb{R}^{\frac{H}{8} \times \frac{W}{8} \times 1}$. These operations are represented as $F(\cdot)$ in Fig. 3. Next, we calculate the Hadamard product between K and T_2' . This operation assigns different weights to different pixels, increasing the weight of edge pixels. After that, we use an adaptive pooling operation to reduce the displacement of features and apply a center crop on it to obtain the feature map $V \in \mathbb{R}^{4 \times 4 \times 16}$. In summary, the process can

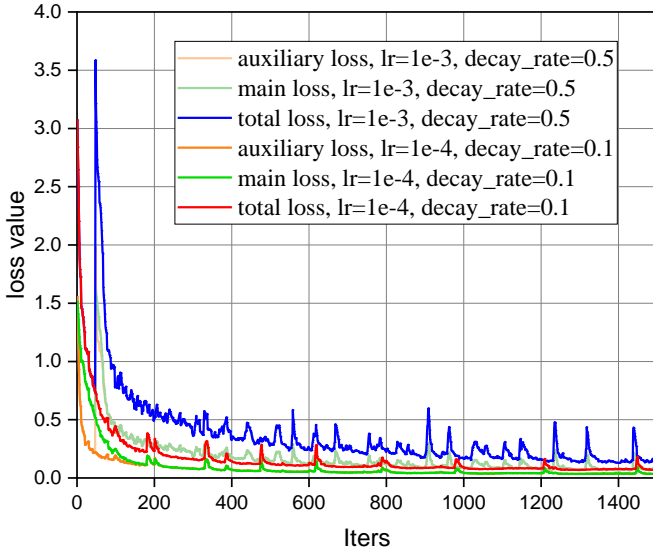


Fig. 4. Loss curves under different training parameter settings.

be formulated as follows:

$$V = \text{AP}(K \odot F(W_g(T_2))), \quad (7)$$

where $\text{AP}(\cdot)$ denotes the pooling and crop operations.

Then, we establish the correlation between each pixel in V and K through an inner product, which is written as follows:

$$f = \sigma(V^T \otimes K), \quad (8)$$

where " \otimes " denotes the inner product operation. V^T is the transpose of V and f is the correlation attention map.

After obtaining the correlation attention map f , we multiply it with the feature map Q , and the result features are fed to the graph convolutional layer [86] $\text{GCN}(\cdot)$, leading to $G \in \mathbb{R}^{4 \times 4 \times 16}$. Same to [86], we calculate the inner product between f and G as Eqn. 9, reconstructing the graph domain features into the original structural features:

$$Y' = f^T \otimes \text{GCN}(f^T \otimes Q). \quad (9)$$

The reconstructed feature map Y' is adjusted to the same channel sizes with Y by a convolutional layer $W_z(\cdot)$ with 1×1 kernel size, and then combined with the feature T_1 to obtain the final output $Z \in \mathbb{R}^{\frac{H}{8} \times \frac{W}{8} \times 32}$ of the SAM. Eqn. 10 summarizes the details of this process:

$$Z = T_1 + W_z(Y'). \quad (10)$$

F. Loss Function

Our loss function can be formulated as Eqn. 11:

$$\mathcal{L} = \mathcal{L}_{\text{main}} + \mathcal{L}_{\text{aux}}, \quad (11)$$

where $\mathcal{L}_{\text{main}}$ and \mathcal{L}_{aux} are the main loss and auxiliary loss, respectively. The main loss $\mathcal{L}_{\text{main}}$ is calculated between the final segmentation result P_2 and ground truth G , which can be written as:

$$\mathcal{L}_{\text{main}} = \mathcal{L}_{\text{IoU}}^w(P_2, G) + \mathcal{L}_{\text{BCE}}^w(P_2, G). \quad (12)$$

TABLE II
PARAMETER SETTING DURING THE TRAINING STAGE.

Optimizer	Learning Rate (lr)	Multi-scale	Clip
AdamW	1e-4	[0.75,1,1.25]	0.5
Decay rate	Weight decay	Epochs	Input Size
0.1	1e-4	100	352×352

The auxiliary loss \mathcal{L}_{aux} is calculated between the intermediate result P_1 from the CFM and ground truth G , which can be formulated as:

$$\mathcal{L}_{\text{aux}} = \mathcal{L}_{\text{IoU}}^w(P_1, G) + \mathcal{L}_{\text{BCE}}^w(P_1, G). \quad (13)$$

$\mathcal{L}_{\text{IoU}}^w(\cdot)$ and $\mathcal{L}_{\text{BCE}}^w(\cdot)$ are the weighted intersection over union (IoU) loss [88] and weighted binary cross entropy (BCE) loss [88], which restrict the prediction map in terms of the global structure (object-level) and local details (pixel-level) perspectives. Unlike the standard BCE loss function, which treats all pixels equally, $\mathcal{L}_{\text{BCE}}^w(\cdot)$ considers the importance of each pixel and assigns higher weights to hard pixels. Furthermore, compared to the standard IoU loss, $\mathcal{L}_{\text{IoU}}^w(\cdot)$ pays more attention to the hard pixels.

G. Implementation Details

We implement our Polyp-PVT with the PyTorch framework and use a Tesla P100 to accelerate the calculations. Considering the differences in the sizes of each polyp image, we adopt a multi-scale strategy [5], [41] in the training stage. The hyperparameter details are as follows. To update the network parameters, we use the AdamW [89] optimizer, which is widely used in transformer networks [71]–[73]. The learning rate is set to 1e-4 and the weight decay is adjusted to 1e-4 too. Further, we resize the input images to 352×352 with a mini-batch size of 16 for 100 epochs. More details about the training loss curves, parameter setting, and network parameters are shown in Fig. 4, Tab. II, and Tab. III, respectively. The total training time is nearly 3 hours to achieve the best (*e.g.*, 30 epochs) performance. For testing, we only resize the images to 352×352 without any post-processing optimization strategies.

IV. EXPERIMENTS

A. Evaluation Metrics

We employ six widely-used evaluation metrics, including Dice [90], IoU, mean absolute error (MAE), weighted F-measure (F_β^w) [91], S-measure (S_α) [92], and E-measure (E_ξ) [93], [94] to evaluate the model performances. Among these metrics, Dice and IoU are similarity measures at the regional level, which mainly focus on the internal consistency of segmented objects. Here, we report the mean value of Dice and IoU, denoted as mDic and mIoU, respectively. MAE is a pixel-by-pixel comparison indicator that represents the average value of the absolute error between the predicted value and the true value. Weighted F-measure (F_β^w) comprehensively considers the recall and precision and eliminates the effect of considering each pixel equally in conventional indicators. S-measure (S_α) focuses on the structural similarity of target prospects at the

TABLE III
NETWORK PARAMETERS OF EACH MODULE. NOTE THAT THE ENCODER PARAMETERS ARE THE SAME AS PVT WITHOUT ANY CHANGES. BASICCONV2D AND CONV2D WITH THE PARAMETERS [IN_CHANNEL, OUT_CHANNEL, KERNEL_SIZE, PADDING] AND GCN [NUM_STATE, NUM_NODE].

Encoder		SAM	
patch_size	[4]	AvgPool2d	[6]
embed_dims	[64, 128, 320, 512]	Conv2d	[32,16,1,1]
num_heads	[1, 2, 5, 8]	Conv2d	[32,16,1,1]
mlp_ratios	[8, 8, 4, 4]	Conv2d	[16,32,1,1]
depths	[3, 4, 18, 3]	GCN	[16,16]
sr_ratios	[8, 4, 2, 1]	BasicConv2d	[64,32,1,0]
drop_rate	[0]		
drop_path_rate	[0.1]		
CFM		CIM	
BasicConv2d	[32,32,3,1]	AvgPool2d	[1]
BasicConv2d	[32,32,3,1]	AvgPool2d	[1]
BasicConv2d	[32,32,3,1]	Conv2d	[64,4,1,0]
BasicConv2d	[32,32,3,1]	ReLU	
BasicConv2d	[64,64,3,1]	Conv2d	[4,64,1,0]
BasicConv2d	[64,64,3,1]	Sigmoid	
BasicConv2d	[96,96,3,1]	Conv2d	[2,1,7,3]
BasicConv2d	[96,32,3,1]	Sigmoid	

region and object level. E-measure (E_ξ) is used to evaluate the segmentation results at the pixel and image level. We report the mean and max value of E-measure, denoted as mE_ξ and $maxE_\xi$, respectively. The evaluation toolbox is derived from <https://github.com/DengPingFan/PraNet>.

B. Datasets and Compared Models

Datasets. Following the experimental setups in PraNet [5], we adopt five challenging public datasets, including Kvasir-SEG [13], ClinicDB [8], ColonDB [10], Endoscene [14] and ETIS [9] to verify the effectiveness of our framework.

Models. We collect several open source models from the field of polyp segmentation, for a total of nine comparative models, including U-Net [4], UNet++ [28], PraNet [5], SFA [95], MSEG [41], ACSNet [49], DCRNet [44], EU-Net [52] and SANet [7]. For a fair comparison, we use their open-source codes to evaluate the same training and testing sets. Note that the SFA results are generated using the released test model.

C. Analysis of Learning Ability

Settings. We use the ClinicDB and Kvasir-SEG datasets to evaluate the learning ability of the proposed model. ClinicDB contains 612 images, which are extracted from 31 colonoscopy videos. Kvasir-SEG is collected from the polyp class in the Kvasir dataset and includes 1,000 polyp images. Following PraNet, we adopt the same 900 and 548 images from ClinicDB and Kvasir-SEG datasets as the training set, and the remaining 64 and 100 images are employed as the respective test sets.

Results. As can be seen in Tab. IV, our model is superior to the current methods, demonstrating that it has a better learning ability. On the Kvasir-SEG dataset, the mDic score of our model is 1.3% higher than that of the second-best model, SANet, and 1.9% higher than that of PraNet. On the ClinicDB

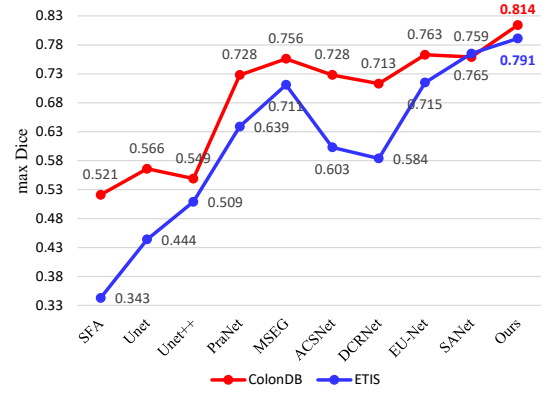


Fig. 5. Evaluation of model generalization ability. We provide the max Dice results on ColonDB and ETIS.

dataset, the mDic score of our model is 2.1% higher than that of SANet and 3.8% higher than that of PraNet.

D. Analysis of Generalization Ability

Settings. To verify the generalization performance of the model, we test it on three unseen (*i.e.*, Polycentric) datasets, namely ETIS, ColonDB, and EndoScene. There are 196 images in ETIS, 380 images in ColonDB, and 60 images in EndoScene. It is worth noting that the images in these datasets belong to different medical centers. In other words, the model has not seen their training data, which is different from the verification methods of ClinicDB and Kvasir-SEG.

Results. The results are shown in Tab. VI and Tab. V. As can be seen, our Polyp-PVT achieves a good generalization performance compared with the existing models. And our model generalizes easily to multicentric (or unseen) data with different domains/distributions. On ColonDB, it is ahead of the second-best SANet and classical PraNet by 5.5% and 9.6%, respectively. On ETIS, we exceed the SANet and PraNet by 3.7% and 15.9%, respectively. In addition, on EndoScene, our model is better than SANet and PraNet by 1.2% and 2.9%, respectively. Moreover, to prove the generalization ability of Polyp-PVT, we present the max Dice results in Fig. 5, where our model shows a steady improvement on both ColonDB and ETIS. In addition, we show the standard deviation (SD) of the mean dice (mDic) between our model and others in Tab. VII. As seen, there is not much difference in SD between our model and the comparison model, and they are both stable and balanced.

E. Qualitative Analysis

Fig. 6 and Fig. 7 show the visualization results of our model and the compared models. We find that our results have two advantages.

- Our model is able to adapt to data under different conditions. That is, it maintains a stable recognition and segmentation ability under different acquisition environments (different lighting, contrast, reflection, motion blur, small objects, and rotation).
- The model segmentation results have internal consistency and predicted edges are closer to the ground-truth labels.

TABLE IV
QUANTITATIVE RESULTS OF THE TEST DATASETS, *i.e.*, KVASIR-SEG AND CLINICDB.

Model	Kvasir-SEG [13]							ClinicDB [8]						
	mDic	mIoU	F_{β}^w	S_{α}	mE_{ξ}	$maxE_{\xi}$	MAE	mDic	mIoU	F_{β}^w	S_{α}	mE_{ξ}	$maxE_{\xi}$	MAE
MICCAI'15 U-Net	0.818	0.746	0.794	0.858	0.881	0.893	0.055	0.823	0.755	0.811	0.889	0.913	0.954	0.019
DLMIA'18 UNet++	0.821	0.743	0.808	0.862	0.886	0.909	0.048	0.794	0.729	0.785	0.873	0.891	0.931	0.022
MICCAI'19 SFA	0.723	0.611	0.670	0.782	0.834	0.849	0.075	0.700	0.607	0.647	0.793	0.840	0.885	0.042
arXiv'21 MSEG	0.897	0.839	0.885	0.912	0.942	0.948	0.028	0.909	0.864	0.907	0.938	0.961	0.969	0.007
arXiv'21 DCRNet	0.886	0.825	0.868	0.911	0.933	0.941	0.035	0.896	0.844	0.890	0.933	0.964	0.978	0.010
MICCAI'20 ACSNet	0.898	0.838	0.882	0.920	0.941	0.952	0.032	0.882	0.826	0.873	0.927	0.947	0.959	0.011
MICCAI'20 PraNet	0.898	0.840	0.885	0.915	0.944	0.948	0.030	0.899	0.849	0.896	0.936	0.963	0.979	0.009
CRV'21 EU-Net	0.908	0.854	0.893	0.917	0.951	0.954	0.028	0.902	0.846	0.891	0.936	0.959	0.965	0.011
MICCAI'21 SANet	0.904	0.847	0.892	0.915	0.949	0.953	0.028	0.916	0.859	0.909	0.939	0.971	0.976	0.012
Polyp-PVT (Ours)	0.917	0.864	0.911	0.925	0.956	0.962	0.023	0.937	0.889	0.936	0.949	0.985	0.989	0.006

TABLE V
QUANTITATIVE RESULTS OF THE TEST DATASETS COLONDB AND ETIS. THE SFA RESULT IS GENERATED USING THE PUBLISHED CODE.

Model	ColonDB [10]							ETIS [9]						
	mDic	mIoU	F_{β}^w	S_{α}	mE_{ξ}	$maxE_{\xi}$	MAE	mDic	mIoU	F_{β}^w	S_{α}	mE_{ξ}	$maxE_{\xi}$	MAE
MICCAI'15 U-Net	0.512	0.444	0.498	0.712	0.696	0.776	0.061	0.398	0.335	0.366	0.684	0.643	0.740	0.036
DLMIA'18 UNet++	0.483	0.410	0.467	0.691	0.680	0.760	0.064	0.401	0.344	0.390	0.683	0.629	0.776	0.035
MICCAI'19 SFA	0.469	0.347	0.379	0.634	0.675	0.764	0.094	0.297	0.217	0.231	0.557	0.531	0.632	0.109
MICCAI'20 ACSNet	0.716	0.649	0.697	0.829	0.839	0.851	0.039	0.578	0.509	0.530	0.754	0.737	0.764	0.059
arXiv'21 MSEG	0.735	0.666	0.724	0.834	0.859	0.875	0.038	0.700	0.630	0.671	0.828	0.854	0.890	0.015
arXiv'21 DCRNet	0.704	0.631	0.684	0.821	0.840	0.848	0.052	0.556	0.496	0.506	0.736	0.742	0.773	0.096
MICCAI'20 PraNet	0.712	0.640	0.699	0.820	0.847	0.872	0.043	0.628	0.567	0.600	0.794	0.808	0.841	0.031
CRV'21 EU-Net	0.756	0.681	0.730	0.831	0.863	0.872	0.045	0.687	0.609	0.636	0.793	0.807	0.841	0.067
MICCAI'21 SANet	0.753	0.670	0.726	0.837	0.869	0.878	0.043	0.750	0.654	0.685	0.849	0.881	0.897	0.015
Polyp-PVT (Ours)	0.808	0.727	0.795	0.865	0.913	0.919	0.031	0.787	0.706	0.750	0.871	0.906	0.910	0.013

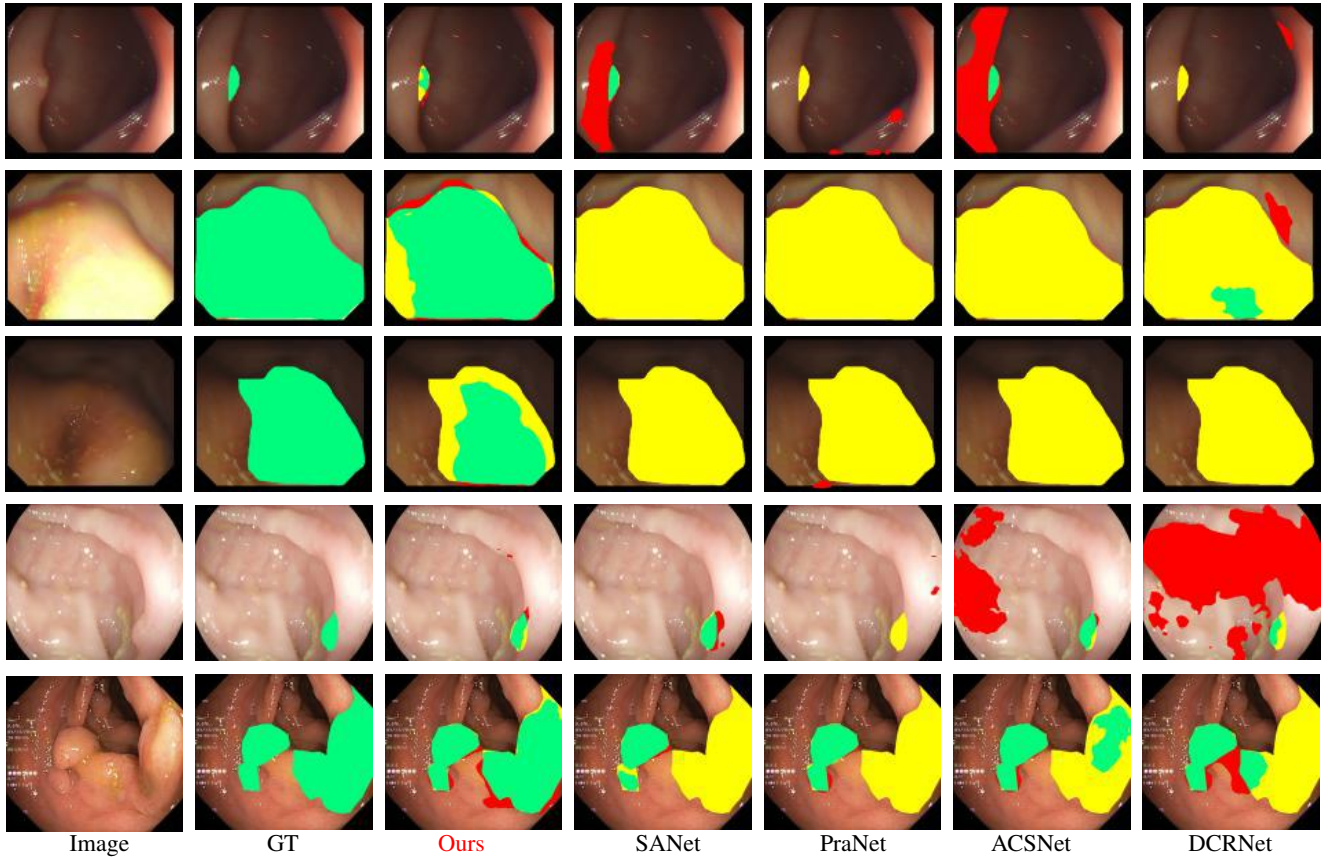


Fig. 6. Visualization results with the current models. Green indicates a correct polyp. Yellow is the missed polyp. Red is the wrong prediction. As we can see, the proposed model can accurately locate and segment polyps, regardless of size.

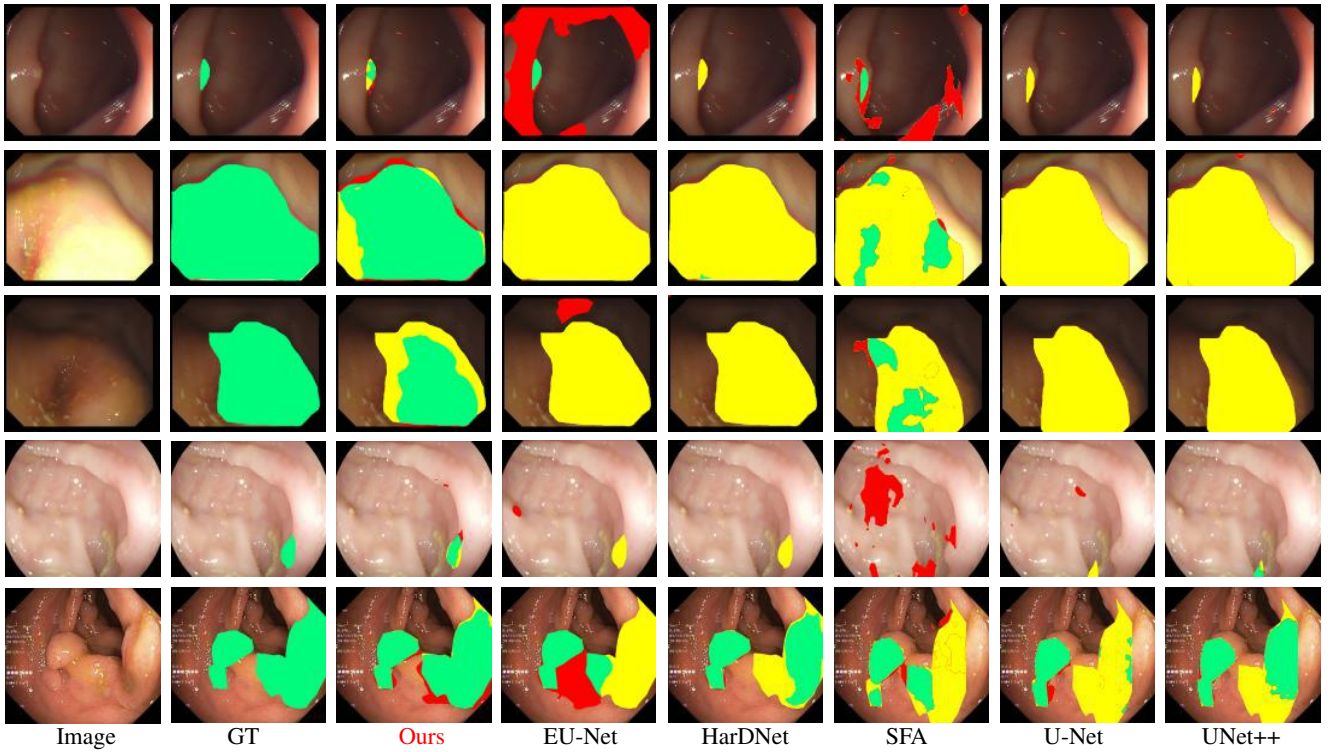


Fig. 7. Visualization results with the current models.

TABLE VI

QUANTITATIVE RESULTS OF THE TEST DATASET ENDOSCENE. THE SFA RESULT IS GENERATED USING THE PUBLISHED CODE.

Model	Endoscene [14]						
	mDic	mIoU	F_{β}^w	S_{α}	mE_{ξ}	$maxE_{\xi}$	MAE
U-Net	0.710	0.627	0.684	0.843	0.847	0.875	0.022
UNet++	0.707	0.624	0.687	0.839	0.834	0.898	0.018
SFA	0.467	0.329	0.341	0.640	0.644	0.817	0.065
MSEG	0.874	0.804	0.852	0.924	0.948	0.957	0.009
ACSNet	0.863	0.787	0.825	0.923	0.939	0.968	0.013
DCRNet	0.856	0.788	0.830	0.921	0.943	0.960	0.010
PraNet	0.871	0.797	0.843	0.925	0.950	0.972	0.010
EU-Net	0.837	0.765	0.805	0.904	0.919	0.933	0.015
SANet	0.888	0.815	0.859	0.928	0.962	0.972	0.008
Polyp-PVT	0.900	0.833	0.884	0.935	0.973	0.981	0.007

We also provide FROC curves on ColonDB in Fig. 8, and our result is at the top, indicating that our effect achieves the best.

F. Ablation Study

We describe in detail the effectiveness of each component on the overall model. The training, testing, and hyperparameter settings are the same as mentioned in Sec. III-G. The results are shown in Tab. VIII.

Components. We use PVTv2 [72] as our baseline (Bas.) and evaluate module effectiveness by removing or replacing components from the complete Polyp-PVT and comparing the variants with the standard version. The standard version is denoted as “Polyp-PVT (PVT+CFM+CIM+SAM)”, where “CFM”, “CIM” and “SAM” indicate the usage of the CFM, CIM, and SAM, respectively.

Effectiveness of CFM. To analyze the effectiveness of the CFM, a version of “Polyp-PVT (w/o CFM)” is trained.

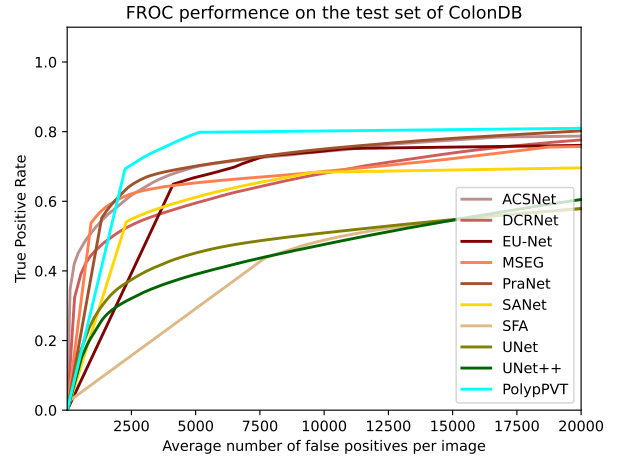


Fig. 8. FROC curves of different methods on ColonDB.

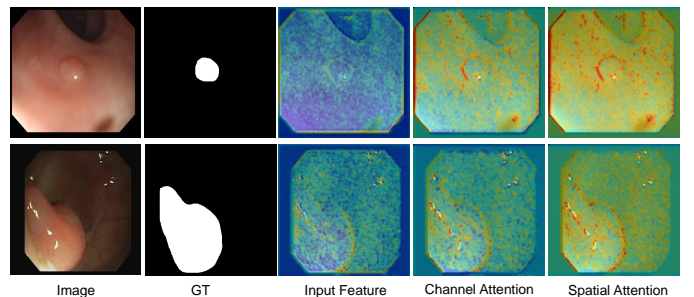


Fig. 9. Visualization of the feature map in the CIM module.

TABLE VII
THE STANDARD DEVIATION (SD) OF THE MEAN DICE (mDic) OF OUR MODEL AND THE COMPARISON MODELS.

Datasets	Kvasir-SEG	ClinicDB	ColonDB	ETIS	Endoscene
Metrics	mDic \pm SD	mDic \pm SD	mDic \pm SD	mDic \pm SD	mDic \pm SD
MICCAI'15 U-Net	.818 \pm .039	.823 \pm .047	.483 \pm .034	.398 \pm .033	.710 \pm .049
DLMIA'18 UNet++	.821 \pm .040	.794 \pm .044	.456 \pm .037	.401 \pm .057	.707 \pm .053
MICCAI'19 SFA	.723 \pm .052	.701 \pm .054	.444 \pm .037	.297 \pm .025	.468 \pm .050
arXiv'21 MSEG	.897 \pm .041	.910 \pm .048	.735 \pm .039	.700 \pm .039	.874 \pm .051
MICCAI'20 ACSNet	.898 \pm .045	.882 \pm .048	.716 \pm .040	.578 \pm .035	.863 \pm .055
arXiv'21 DCRNet	.886 \pm .043	.896 \pm .049	.704 \pm .039	.556 \pm .039	.857 \pm .052
MICCAI'20 PraNet	.898 \pm .041	.899 \pm .048	.712 \pm .038	.628 \pm .036	.871 \pm .051
CRV'21 EU-Net	.908 \pm .042	.902 \pm .048	.756 \pm .040	.687 \pm .039	.837 \pm .049
MICCAI'21 SANet	.904 \pm .042	.916 \pm .049	.752 \pm .040	.750 \pm .047	.888 \pm .054
Polyp-PVT (Ours)	.917 \pm .042	.937 \pm .050	.808 \pm .043	.787 \pm .044	.900 \pm .052

TABLE VIII
QUANTITATIVE RESULTS FOR ABLATION STUDIES.

Dataset	Metric	Bas.	w/o CFM	w/o CIM	w/o SAM	Final
Endoscene	mDic	0.869	0.892	0.882	0.874	0.900
	mIoU	0.792	0.826	0.808	0.801	0.833
ClinicDB	mDic	0.903	0.915	0.930	0.930	0.937
	mIoU	0.847	0.865	0.881	0.877	0.889
ColonDB	mDic	0.796	0.802	0.805	0.779	0.808
	mIoU	0.707	0.721	0.724	0.696	0.727
ETIS	mDic	0.759	0.771	0.785	0.778	0.787
	mIoU	0.668	0.690	0.711	0.693	0.706
Kvasir-SEG	mDic	0.910	0.922	0.910	0.910	0.917
	mIoU	0.856	0.872	0.858	0.853	0.864

TABLE IX
ABLATION STUDY OF GCN IN THE SAM MODULE.

Setting	Endoscene	ClinicDB	ColonDB	ETIS	Kvasir-SEG
w/o GCN	0.876	0.928	0.784	0.725	0.894
w/ Conv	0.894	0.919	0.787	0.742	0.909
w/ GCN	0.900	0.937	0.808	0.787	0.917

Tab. VIII shows that the model without the CFM drops sharply on all five datasets compared to the standard Polyp-PVT. In particular, the mDic is reduced from 0.937 to 0.915 on ClinicDB.

Effectiveness of CIM. To demonstrate the ability of the CIM, we also remove it from Polyp-PVT, denoting this as “Polyp-PVT (w/o CIM)”. As shown in Tab. VIII, this variant performs worse than the overall Polyp-PVT. Specifically, removing the CIM causes the mDic to decrease by 1.8% on Endoscene. Meanwhile, it is obvious that the lack of the CIM introduces significant noise (please refer to Fig. 10). In order to further explore the internal of CIM, the feature visualizations of the two main configurations inside the CIM are shown in Fig 9. It can be seen that the low-level features have a large amount of detailed information. Still, the differences between polyps and other normal tissues cannot be mined directly from this information. Thanks to the channel attention and spatial attention mechanism, information such as details and edges of polyps can be discerned from a large amount of redundant information.

Effectiveness of SAM. Similarly, we test the effectiveness of the SAM module by removing it from the overall Polyp-PVT and replacing it with an element-wise addition operation,

TABLE X
ABOUT THE ABLATION EXPERIMENTS OF THE POWERFUL ROTATION ADAPTABILITY. ALL EXPERIMENTS ARE UNDER THE CONDITION OF LARGE ROTATION (15 DEGREES).

Setting	Endoscene	ClinicDB	ColonDB	ETIS	Kvasir-SEG
w/o GCN	0.857	0.909	0.756	0.667	0.894
w/ Conv	0.865	0.898	0.789	0.719	0.893
w/ GCN	0.874	0.929	0.806	0.744	0.915

which is denoted as “Polyp-PVT (w/o SAM)”. The performance of the complete Polyp-PVT shows an improvement of 2.9% and 3.1% in terms of mDic and mIoU, respectively, on ColonDB. Fig. 10 shows the benefits of SAM more intuitively. It is found that the lack of the SAM leads to more detailed errors or even missed inspections. As reported in Tab IX, we add more results on the GCN in the SAM module. The experimental results further illustrate that GCN plays a key role. The effect of the lack of GCN is significantly reduced, and the effect is improved after replacing it with convolution. Still, GCN can significantly exceed the capabilities of the convolution module. The experimental results also verified the importance of GCN’s large receptive field and rotation insensitivity to polyp segmentation. The rotational robustness of GCN is stronger than convolutions. As shown in Tab X, under the condition of large rotation (15 degrees), GCN has better adaptability to image rotation than convolutions. To further explore the role of SAM, we visualized P1 and P2, and the results of P1 and P2 are shown in Fig 11. Compared with P1, P2 has higher reliability in error recognition and identification of uncertain regions. This is mainly due to the large number of low-level details collected by CIM and mining local pixels and global semantic cues from the polyp area of SAM.

G. Video Polyp Segmentation

To validate the superiority of the proposed model, we conduct experiments on the video polyp segmentation datasets. For a fair comparison, we re-train our model with the same training datasets and use the same testing set as PNS-Net [64], [97]. We compare our model on three standard benchmarks (*i.e.*, CVC-300-TV [96], CVC-612-T [8], and CVC-612-V [8]) against six cutting-edge approaches, including U-Net [4],

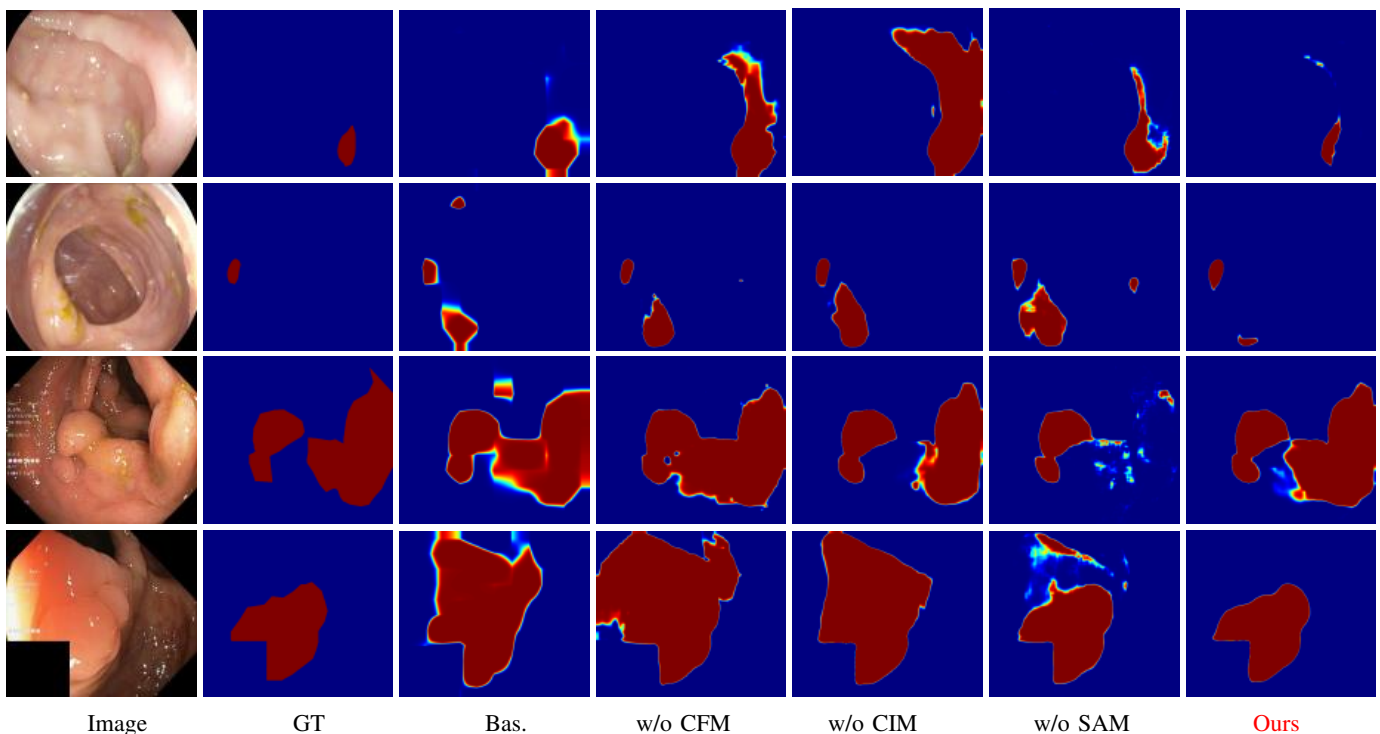


Fig. 10. Visualization of the ablation study results, which are converted from the output into heat maps. As can be seen, removing any module leads to missed or incorrectly detected results.

TABLE XI
THE RESULT OF VIDEO POLYP SEGMENTATION ON THE *i.e.*, CVC-612-T AND CVC-612-V.

Model	CVC-612-T [8]							CVC-612-V [8]						
	mDic	mIoU	F_{β}^w	S_{α}	mE_{ξ}	$maxE_{\xi}$	MAE	mDic	mIoU	F_{β}^w	S_{α}	mE_{ξ}	$maxE_{\xi}$	MAE
MICCAI'15 U-Net	0.711	0.618	0.694	0.810	0.836	0.853	0.058	0.709	0.597	0.680	0.826	0.855	0.872	0.023
TMI'19 UNet++	0.697	0.603	0.688	0.800	0.817	0.865	0.059	0.668	0.557	0.642	0.805	0.830	0.846	0.025
ISM'19 ResUNet++	0.616	0.512	0.604	0.727	0.758	0.760	0.084	0.750	0.646	0.717	0.829	0.877	0.879	0.023
MICCAI'20 ACSNet	0.780	0.697	0.772	0.838	0.864	0.866	0.053	0.801	0.710	0.765	0.847	0.887	0.890	0.054
MICCAI'20 PraNet	0.833	0.767	0.834	0.886	0.904	0.926	0.038	0.857	0.793	0.855	0.915	0.936	0.965	0.013
MICCAI'21 PNS-Net	0.837	0.765	0.838	0.903	0.903	0.923	0.038	0.851	0.769	0.836	0.923	0.944	0.962	0.012
Polyp-PVT (Ours)	0.846	0.776	0.850	0.895	0.908	0.926	0.037	0.882	0.810	0.874	0.924	0.963	0.967	0.012

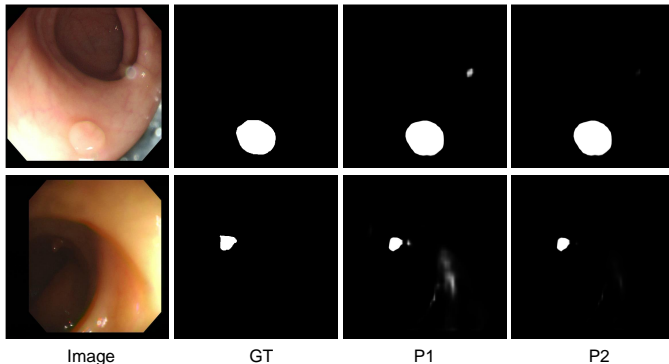


Fig. 11. visualization of the P1 and P2 predictions.

TABLE XII
VIDEO POLYP SEGMENTATION RESULTS ON THE CVC-300-TV.

Model	CVC-300-TV [96]						
	mDic	mIoU	F_{β}^w	S_{α}	mE_{ξ}	$maxE_{\xi}$	MAE
U-Net	0.631	0.516	0.567	0.793	0.826	0.849	0.027
UNet++	0.638	0.527	0.581	0.796	0.831	0.847	0.024
ResUNet++	0.533	0.410	0.469	0.703	0.718	0.720	0.052
ACSNet	0.732	0.627	0.703	0.837	0.871	0.875	0.016
PraNet	0.716	0.624	0.700	0.833	0.852	0.904	0.016
PNS-Net	0.813	0.710	0.778	0.909	0.921	0.942	0.013
Ours	0.880	0.802	0.869	0.915	0.961	0.965	0.011

existing model, PNS-Net, by 3.1% and 6.7% on CVC-612-V and CVC-300-TV, respectively, in terms of mDice.

UNet++ [28], ResUNet++ [29], ACSNet [49], PraNet [5], PNS-Net [64], in Tab. XI and Tab. XII. Note that PNS-Net provides all the prediction maps of the compared methods. As seen, our method is very competitive and far ahead of the best

H. Limitations

Although the proposed Polyp-PVT model surpasses existing algorithms, it still performs poorly in certain cases. We present some failure cases in Fig. 12. As can be seen, one major

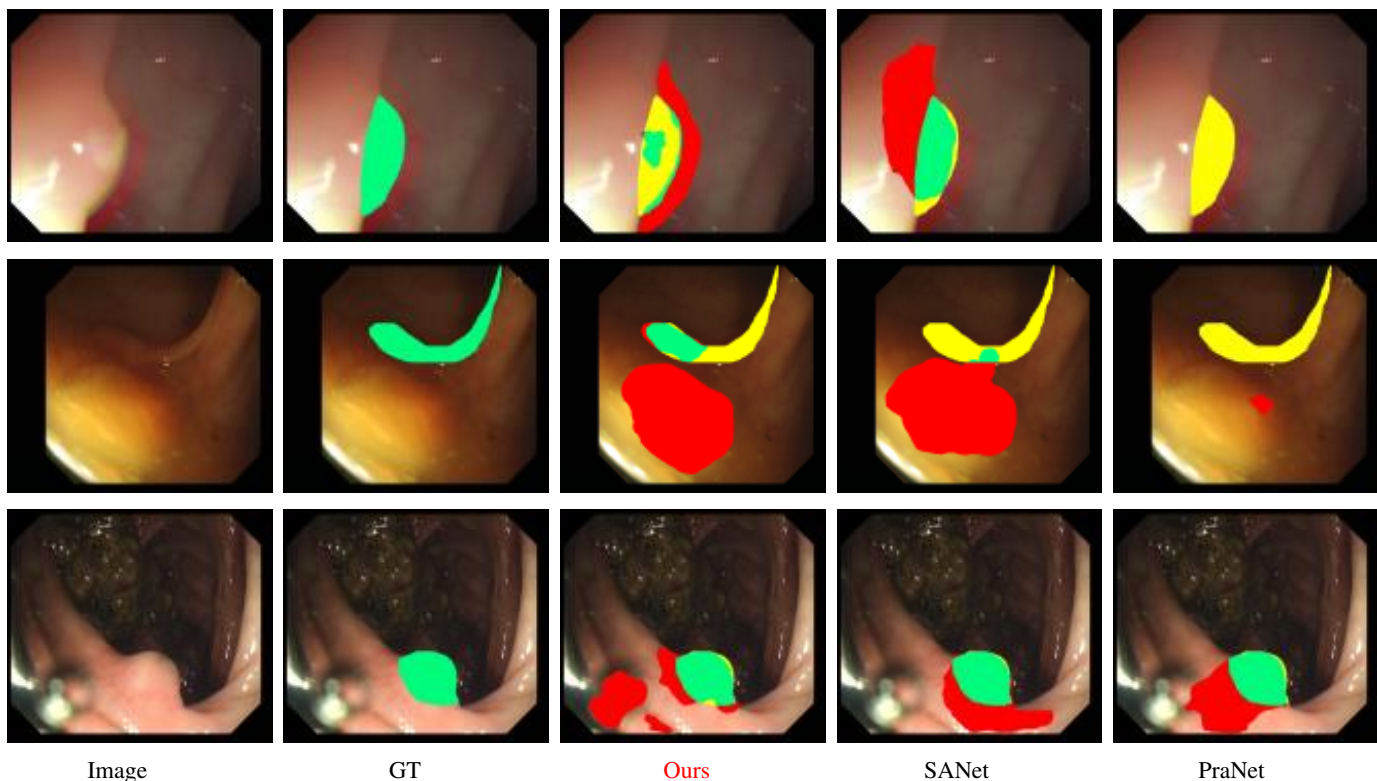


Fig. 12. Visualization of some failure cases. Green indicates a correct polyp. Yellow is the missed polyp. Red is the wrong prediction.

limitation is the inability to detect accurate polyp boundaries with overlapping light and shadow (1st row). Our model can identify the location information of polyps (green mask in 1st row), but it regards the light and shadow part of the edge as the polyp (red mask in 1st row). More deadly, our model incorrectly predicts the reflective point as a polyp (red mask in 2nd and 3rd rows). We notice that the reflective points are very salient in the image. Therefore, we speculate that the prediction may be based on only these points. More importantly, we believe that a simple way is to convert the input image into a gray image, which can eliminate the reflection and overlap of light and shadow to assist the model in judgment.

V. CONCLUSION

In this paper, we propose a new image polyp segmentation framework, named Polyp-PVT, which utilizes a pyramid vision transformer backbone as the encoder to explicitly extract more powerful and robust features. Extensive experiments show that Polyp-PVT consistently outperforms all current cutting-edge models on five challenging datasets without any pre-/post-processing. In particular, for the unseen ColonDB dataset, the proposed model reaches a mean Dice score of above 0.8 for the first time. Interestingly, we also surpass the current cutting-edge PNS-Net in terms of the video polyp segmentation task, demonstrating excellent learning ability. Specifically, we obtain the above-mentioned achievements by introducing three simple components, *i.e.*, a cascaded fusion module (CFM), a camouflage identification module (CIM), and a similarity aggregation module (SAM), which effectively extract high and

low-level cues separately, and effectively fuse them for the final output. We hope this research will stimulate more novel ideas for solving the polyp segmentation task.

REFERENCES

- [1] M. Fiori, P. Musé, and G. Sapiro, "A complete system for candidate polyps detection in virtual colonoscopy," *IJPRAI*, vol. 28, no. 07, p. 1460014, 2014.
- [2] A. V. Mamonov, I. N. Figueiredo, P. N. Figueiredo, and Y.-H. R. Tsai, "Automated polyp detection in colon capsule endoscopy," *IEEE TMI*, vol. 33, no. 7, pp. 1488–1502, 2014.
- [3] O. H. Maghsoudi, "Superpixel based segmentation and classification of polyps in wireless capsule endoscopy," in *IEEE SPMB*, 2017.
- [4] O. Ronneberger, P. Fischer, and T. Brox, "U-net: Convolutional networks for biomedical image segmentation," in *MICCAI*, 2015.
- [5] D.-P. Fan, G.-P. Ji, T. Zhou, G. Chen, H. Fu, J. Shen, and L. Shao, "Pranet: Parallel reverse attention network for polyp segmentation," in *MICCAI*, 2020.
- [6] X. Guo, C. Yang, Y. Liu, and Y. Yuan, "Learn to threshold: Thresholdnet with confidence-guided manifold mixup for polyp segmentation," *IEEE TMI*, vol. 40, no. 4, pp. 1134–1146, 2020.
- [7] J. Wei, Y. Hu, R. Zhang, Z. Li, S. K. Zhou, and S. Cui, "Shallow attention network for polyp segmentation," in *MICCAI*, 2021.
- [8] J. Bernal, F. J. Sánchez, G. Fernández-Esparrach, D. Gil, C. Rodríguez, and F. Vilarino, "Wm-dova maps for accurate polyp highlighting in colonoscopy: Validation vs. saliency maps from physicians," *CMIG*, vol. 43, pp. 99–111, 2015.
- [9] J. Silva, A. Histace, O. Romain, X. Dray, and B. Granado, "Toward embedded detection of polyps in wce images for early diagnosis of colorectal cancer," *IJCARS*, vol. 9, no. 2, pp. 283–293, 2014.
- [10] N. Tajbakhsh, S. R. Gurudu, and J. Liang, "Automated polyp detection in colonoscopy videos using shape and context information," *IEEE TMI*, vol. 35, no. 2, pp. 630–644, 2015.
- [11] D.-P. Fan, G.-P. Ji, M.-M. Cheng, and L. Shao, "Concealed object detection," *IEEE TPAMI*, 2021.
- [12] D.-P. Fan, G.-P. Ji, G. Sun, M.-M. Cheng, J. Shen, and L. Shao, "Camouflaged object detection," in *CVPR*, 2020.

- [13] D. Jha, P. H. Smedsrud, M. A. Riegler, P. Halvorsen, T. de Lange, D. Johansen, and H. D. Johansen, "Kvasir-seg: A segmented polyp dataset," in *MMM*, 2020.
- [14] D. Vázquez, J. Bernal, F. J. Sánchez, G. Fernández-Esparrach, A. M. López, A. Romero, M. Drozdal, and A. Courville, "A benchmark for endoluminal scene segmentation of colonoscopy images," *JHE*, vol. 2017, 2017.
- [15] T. Rahim, M. A. Usman, and S. Y. Shin, "A survey on contemporary computer-aided tumor, polyp, and ulcer detection methods in wireless capsule endoscopy imaging," *CMIG*, p. 101767, 2020.
- [16] K. He, X. Zhang, S. Ren, and J. Sun, "Deep residual learning for image recognition," in *CVPR*, 2016.
- [17] K. Simonyan and A. Zisserman, "Very deep convolutional networks for large-scale image recognition," in *ICLR*, 2015.
- [18] X. Li, W. Wang, X. Hu, and J. Yang, "Selective kernel networks," in *CVPR*, 2019.
- [19] W. Wang, X. Li, T. Lu, and J. Yang, "Mixed link networks," in *IJCAI*, 2018.
- [20] J. Long, E. Shelhamer, and T. Darrell, "Fully convolutional networks for semantic segmentation," in *CVPR*, 2015.
- [21] L. Cai, M. Wu, L. Chen, W. Bai, M. Yang, S. Lyu, and Q. Zhao, "Using guided self-attention with local information for polyp segmentation," in *MICCAI*. Springer, 2022.
- [22] N. K. Tomar, D. Jha, U. Bagci, and S. Ali, "Tganet: Text-guided attention for improved polyp segmentation," in *MICCAI*. Springer, 2022.
- [23] R. Zhang, P. Lai, X. Wan, D.-J. Fan, F. Gao, X.-J. Wu, and G. Li, "Lesion-aware dynamic kernel for polyp segmentation," in *MICCAI*. Springer, 2022.
- [24] J.-H. Shi, Q. Zhang, Y.-H. Tang, and Z.-Q. Zhang, "Polyp-mixer: An efficient context-aware mlp-based paradigm for polyp segmentation," *IEEE TCSVT*, 2022.
- [25] X. Zhao, Z. Wu, S. Tan, D.-J. Fan, Z. Li, X. Wan, and G. Li, "Semi-supervised spatial temporal attention network for video polyp segmentation," in *MICCAI*. Springer, 2022.
- [26] M. Akbari, M. Mohrekehsh, E. Nasr-Esfahani, S. R. Soroushmehr, N. Karimi, S. Samavi, and K. Najarian, "Polyp segmentation in colonoscopy images using fully convolutional network," in *IEEE EMBC*, 2018.
- [27] P. Brandao, O. Zisimopoulos, E. Mazomenos, G. Ciuti, J. Bernal, M. Visentini-Scarzanella, A. Mencias, P. Dario, A. Koulaouzidis, A. Arezzo *et al.*, "Towards a computed-aided diagnosis system in colonoscopy: automatic polyp segmentation using convolution neural networks," *JMRR*, vol. 3, no. 02, p. 1840002, 2018.
- [28] Z. Zhou, M. M. R. Siddiquee, N. Tajbakhsh, and J. Liang, "Unet++: A nested u-net architecture for medical image segmentation," in *DLIA*, 2018.
- [29] D. Jha, P. H. Smedsrud, M. A. Riegler, D. Johansen, T. de Lange, P. Halvorsen, and H. D. Johansen, "Resunet++: An advanced architecture for medical image segmentation," in *IEEE ISM*, 2019.
- [30] X. Sun, P. Zhang, D. Wang, Y. Cao, and B. Liu, "Colorectal polyp segmentation by u-net with dilation convolution," in *IEEE ICMLA*, 2019.
- [31] B. Murugesan, K. Sarveswaran, S. M. Shankaranarayana, K. Ram, J. Joseph, and M. Sivaprakasam, "Psi-net: Shape and boundary aware joint multi-task deep network for medical image segmentation," in *IEEE EMBC*, 2019.
- [32] H. A. Qadir, Y. Shin, J. Solhusvik, J. Bergsland, L. Aabakken, and I. Balasingham, "Polyp detection and segmentation using mask r-cnn: Does a deeper feature extractor cnn always perform better?" in *ISMICT*, 2019.
- [33] K. He, G. Gkioxari, P. Dollár, and R. Girshick, "Mask r-cnn," in *ICCV*, 2017.
- [34] S. Alam, N. K. Tomar, A. Thakur, D. Jha, and A. Rauniyar, "Automatic polyp segmentation using u-net-resnet50," in *MediaEvalW*, 2020.
- [35] D. Banik, K. Roy, D. Bhattacharjee, M. Nasipuri, and O. Krejcar, "Polyp-net: A multimodel fusion network for polyp segmentation," *IEEE TIM*, vol. 70, pp. 1–12, 2020.
- [36] T. Rahim, S. A. Hassan, and S. Y. Shin, "A deep convolutional neural network for the detection of polyps in colonoscopy images," *BSPC*, vol. 68, p. 102654, 2021.
- [37] D. Jha, S. Ali, N. K. Tomar, H. D. Johansen, D. Johansen, J. Rittscher, M. A. Riegler, and P. Halvorsen, "Real-time polyp detection, localization and segmentation in colonoscopy using deep learning," *IEEE Access*, vol. 9, pp. 40496–40510, 2021.
- [38] A. M. A. Ahmed, "Generative adversarial networks for automatic polyp segmentation," in *MediaEvalW*, 2020.
- [39] V. Thambawita, S. Hicks, P. Halvorsen, and M. A. Riegler, "Pyramid-focus-augmentation: Medical image segmentation with step-wise focus," in *MediaEvalW*, 2020.
- [40] N. K. Tomar, D. Jha, S. Ali, H. D. Johansen, D. Johansen, M. A. Riegler, and P. Halvorsen, "Ddanet: Dual decoder attention network for automatic polyp segmentation," in *ICPRW*, 2021.
- [41] C.-H. Huang, H.-Y. Wu, and Y.-L. Lin, "Hardnet-mseg: A simple encoder-decoder polyp segmentation neural network that achieves over 0.9 mean dice and 86 fps," *arXiv preprint arXiv:2101.07172*, 2021.
- [42] P. Chao, C.-Y. Kao, Y.-S. Ruan, C.-H. Huang, and Y.-L. Lin, "Hardnet: A low memory traffic network," in *CVPR*, 2019.
- [43] Y. Zhang, H. Liu, and Q. Hu, "Transfuse: Fusing transformers and cnns for medical image segmentation," in *MICCAI*, 2021.
- [44] Z. Yin, K. Liang, Z. Ma, and J. Guo, "Duplex contextual relation network for polyp segmentation," in *IEEE ISBI*, 2022.
- [45] Z. Xiaoqi, Z. Lihe, and L. Huchuan, "Automatic polyp segmentation via multi-scale subtraction network," in *MICCAI*, 2021.
- [46] Z. Zhou, J. Shin, L. Zhang, S. Gurudu, M. Gotway, and J. Liang, "Fine-tuning convolutional neural networks for biomedical image analysis: actively and incrementally," in *CVPR*, 2017.
- [47] N. Tajbakhsh, J. Y. Shin, S. R. Gurudu, R. T. Hurst, C. B. Kendall, M. B. Gotway, and J. Liang, "Convolutional neural networks for medical image analysis: Full training or fine tuning?" *IEEE TMI*, vol. 35, no. 5, pp. 1299–1312, 2016.
- [48] X. Xie, J. Chen, Y. Li, L. Shen, K. Ma, and Y. Zheng, "Mi²gan: Generative adversarial network for medical image domain adaptation using mutual information constraint," in *MICCAI*, 2020.
- [49] R. Zhang, G. Li, Z. Li, S. Cui, D. Qian, and Y. Yu, "Adaptive context selection for polyp segmentation," in *MICCAI*, 2020.
- [50] N. K. Tomar, "Automatic polyp segmentation using fully convolutional neural network," in *MediaEvalW*, 2020.
- [51] D. Jha, S. Hicks, K. Emanuelsen, H. D. Johansen, D. Johansen, T. de Lange, M. A. Riegler, and P. Halvorsen, "Medico multimedia task at mediaeval 2020: Automatic polyp segmentation," in *MediaEvalW*, 2020.
- [52] K. Patel, A. M. Bur, and G. Wang, "Enhanced u-net: A feature enhancement network for polyp segmentation," in *CRV*, 2021.
- [53] A. Lumini, L. Nanni, and G. Maguolo, "Deep ensembles based on stochastic activation selection for polyp segmentation," in *MIDL*, 2021.
- [54] M. V. Branch and A. S. Carvalho, "Polyp segmentation in colonoscopy images using u-net-mobilenetv2," *arXiv preprint arXiv:2103.15715*, 2021.
- [55] R. Khadga, D. Jha, S. Ali, S. Hicks, V. Thambawita, M. A. Riegler, and P. Halvorsen, "Few-shot segmentation of medical images based on meta-learning with implicit gradients," *arXiv preprint arXiv:2106.03223*, 2021.
- [56] D. V. Sang, T. Q. Chung, P. N. Lan, D. V. Hang, D. Van Long, and N. T. Thuy, "Ag-curesnest: A novel method for colon polyp segmentation," in *IEEE RIVF*, 2021.
- [57] C. Yang, X. Guo, M. Zhu, B. Ibragimov, and Y. Yuan, "Mutual-prototype adaptation for cross-domain polyp segmentation," *IEEE JBHI*, 2021.
- [58] D. Jha, P. H. Smedsrud, D. Johansen, T. de Lange, H. D. Johansen, P. Halvorsen, and M. A. Riegler, "A comprehensive study on colorectal polyp segmentation with resunet++, conditional random field and test-time augmentation," *IEEE JBHI*, vol. 25, no. 6, pp. 2029–2040, 2021.
- [59] D. Jha, N. K. Tomar, S. Ali, M. A. Riegler, H. D. Johansen, D. Johansen, T. de Lange, and P. Halvorsen, "Nanonet: Real-time polyp segmentation in video capsule endoscopy and colonoscopy," in *IEEE CBMS*, 2021.
- [60] S. Li, X. Sui, X. Luo, X. Xu, L. Yong, and R. S. M. Goh, "Medical image segmentation using squeeze-and-expansion transformers," in *IJCAI*, 2021.
- [61] T. Kim, H. Lee, and D. Kim, "Uacnet: Uncertainty augmented context attention for polyp segmentation," in *ACM MM*, 2021.
- [62] V. Thambawita, S. A. Hicks, P. Halvorsen, and M. A. Riegler, "Divergentnets: Medical image segmentation by network ensemble," in *ISBI & EndoCV*, 2021.
- [63] G. Xiaoqing, Y. Chen, and Y. Yixuan, "Dynamic-weighting hierarchical segmentation network for medical images," *MIA*, p. 102196, 2021.
- [64] G.-P. Ji, Y.-C. Chou, D.-P. Fan, G. Chen, D. Jha, H. Fu, and L. Shao, "Pns-net: Progressively normalized self-attention network for video polyp segmentation," in *MICCAI*, 2021.
- [65] A. Vaswani, N. Shazeer, N. Parmar, J. Uszkoreit, L. Jones, A. N. Gomez, L. Kaiser, and I. Polosukhin, "Attention is all you need," in *NeurIPS*, 2017.
- [66] A. Dosovitskiy, L. Beyer, A. Kolesnikov, D. Weissenborn, X. Zhai, T. Unterthiner, M. Dehghani, M. Minderer, G. Heigold, S. Gelly *et al.*,

- “An image is worth 16x16 words: Transformers for image recognition at scale,” in *ICLR*, 2021.
- [67] Z. Pan, B. Zhuang, J. Liu, H. He, and J. Cai, “Scalable visual transformers with hierarchical pooling,” in *ICCV*, 2021.
- [68] B. Heo, S. Yun, D. Han, S. Chun, J. Choe, and S. J. Oh, “Rethinking spatial dimensions of vision transformers,” in *ICCV*, 2021.
- [69] L. Yuan, Y. Chen, T. Wang, W. Yu, Y. Shi, Z. Jiang, F. E. Tay, J. Feng, and S. Yan, “Tokens-to-token vit: Training vision transformers from scratch on imagenet,” in *ICCV*, 2021.
- [70] K. Han, A. Xiao, E. Wu, J. Guo, C. Xu, and Y. Wang, “Transformer in transformer,” *Advances in Neural Information Processing Systems*, vol. 34, pp. 15 908–15 919, 2021.
- [71] W. Wang, E. Xie, X. Li, D.-P. Fan, K. Song, D. Liang, T. Lu, P. Luo, and L. Shao, “Pyramid vision transformer: A versatile backbone for dense prediction without convolutions,” in *ICCV*, 2021.
- [72] W. Wang, E. Xie, X. Li, D.-P. Fan, K. Song, D. Liang, T. Lu, P. Luo, and L. Shao, “Pvt v2: Improved baselines with pyramid vision transformer,” *CVMJ*, vol. 8, no. 3, pp. 415–424, 2022.
- [73] Z. Liu, Y. Lin, Y. Cao, H. Hu, Y. Wei, Z. Zhang, S. Lin, and B. Guo, “Swin transformer: Hierarchical vision transformer using shifted windows,” in *ICCV*, 2021.
- [74] H. Wu, B. Xiao, N. Codella, M. Liu, X. Dai, L. Yuan, and L. Zhang, “Cvt: Introducing convolutions to vision transformers,” in *ICCV*, 2021.
- [75] W. Xu, Y. Xu, T. Chang, and Z. Tu, “Co-scale conv-attentional image transformers,” in *ICCV*, 2021.
- [76] X. Chu, Z. Tian, Y. Wang, B. Zhang, H. Ren, X. Wei, H. Xia, and C. Shen, “Twins: Revisiting the design of spatial attention in vision transformers,” *Advances in Neural Information Processing Systems*, vol. 34, pp. 9355–9366, 2021.
- [77] B. Graham, A. El-Nouby, H. Touvron, P. Stock, A. Joulin, H. Jégou, and M. Douze, “Levit: a vision transformer in convnet’s clothing for faster inference,” in *ICCV*, 2021.
- [78] S. Bhojanapalli, A. Chakrabarti, D. Glasner, D. Li, T. Unterthiner, and A. Veit, “Understanding robustness of transformers for image classification,” in *ICCV*, 2021.
- [79] E. Xie, W. Wang, Z. Yu, A. Anandkumar, J. M. Alvarez, and P. Luo, “Segformer: Simple and efficient design for semantic segmentation with transformers,” *Advances in Neural Information Processing Systems*, vol. 34, pp. 12 077–12 090, 2021.
- [80] Z. Wu, L. Su, and Q. Huang, “Cascaded partial decoder for fast and accurate salient object detection,” in *CVPR*, 2019.
- [81] S. Ioffe and C. Szegedy, “Batch normalization: Accelerating deep network training by reducing internal covariate shift,” in *ICML*, 2015.
- [82] X. Glorot, A. Bordes, and Y. Bengio, “Deep sparse rectifier neural networks,” in *AISTATS*, 2011.
- [83] S. Woo, J. Park, J.-Y. Lee, and I. So Kweon, “Cbam: Convolutional block attention module,” in *ECCV*, 2018.
- [84] J. Hu, L. Shen, and G. Sun, “Squeeze-and-excitation networks,” in *CVPR*, 2018.
- [85] X. Wang, R. Girshick, A. Gupta, and K. He, “Non-local neural networks,” in *CVPR*, 2018.
- [86] G. Te, Y. Liu, W. Hu, H. Shi, and T. Mei, “Edge-aware graph representation learning and reasoning for face parsing,” in *ECCV*, 2020.
- [87] Y. Lu, Y. Chen, D. Zhao, and J. Chen, “Graph-fcn for image semantic segmentation,” in *ISNN*, 2019.
- [88] J. Wei, S. Wang, and Q. Huang, “F³net: Fusion, feedback and focus for salient object detection,” in *AAAI*, 2020.
- [89] I. Loshchilov and F. Hutter, “Decoupled weight decay regularization,” in *ICLR*, 2019.
- [90] F. Milletari, N. Navab, and S.-A. Ahmadi, “V-net: Fully convolutional neural networks for volumetric medical image segmentation,” in *3DV*, 2016.
- [91] R. Margolin, L. Zelnik-Manor, and A. Tal, “How to evaluate foreground maps?” in *CVPR*, 2014.
- [92] M.-M. Chen and D.-P. Fan, “Structure-measure: A new way to evaluate foreground maps,” *IJCV*, vol. 129, pp. 2622–2638, 2021.
- [93] D.-P. Fan, G.-P. Ji, X. Qin, and M.-M. Cheng, “Cognitive vision inspired object segmentation metric and loss function,” *SSI*, 2021.
- [94] D.-P. Fan, C. Gong, Y. Cao, B. Ren, M.-M. Cheng, and A. Borji, “Enhanced-alignment measure for binary foreground map evaluation,” in *IJCAI*, 2018.
- [95] Y. Fang, C. Chen, Y. Yuan, and K.-y. Tong, “Selective feature aggregation network with area-boundary constraints for polyp segmentation,” in *MICCAI*, 2019.
- [96] J. Bernal, J. Sánchez, and F. Vilarino, “Towards automatic polyp detection with a polyp appearance model,” *PR*, vol. 45, no. 9, pp. 3166–3182, 2012.
- [97] G.-P. Ji, G. Xiao, Y.-C. Chou, D.-P. Fan, K. Zhao, G. Chen, and L. Van Gool, “Video polyp segmentation: A deep learning perspective,” *MIR*, vol. 19, no. 06, pp. 531–549, 2022.



This is your template for Nordic Machine Intelligence

Bo Dong¹, Wenhai Wang² and Jinpeng Li³

1. College of Biomedical Engineering & Instrument Science, Zhejiang University, Zhejiang, China.E
2. Inception Institute of Artificial Intelligence, Abu Dhabi, UAE
3. E-mail any correspondence to: myname@domain.com

Abstract

We present our solutions to the MedAI: Transparency in Medical Image Segmentation, for all the three tasks: polyp segmentation task, instrument segmentation task, transparency task. We use the same pipeline to process the two segmentation tasks of polyps and surgery, and use the same pre-processing and post-processing operations. The key improvement over last year is newer state-of-the-art vision architectures, especially transformers which significantly outperform ConvNets for the medical image segmentation task. Our solution consists of multi-model fusion, and each model uses a transformer as the backbone network. We finished the all the tasks and get the best score of 0.91 in instrument segmentation task and 0.83 in polyp segmentation task. Meanwhile, we provide complete solutions in <https://github.com/dongbo811/MedAI-2021>.

Keywords: artificial intelligence; machine learning; deep learning; robotics

Introduction

Colorectal cancer is one of the deadly cancers in the world. Colonoscopy is the standard treatment to check, locate and remove colorectal polyps. However, it has been shown that the missed diagnosis rate of colorectal polyps during colonoscopy is between 6% and 27%. The use of automatic, accurate and real-time polyp segmentation during colonoscopy can help clinicians eliminate missing lesions and prevent the further development of colorectal cancer.

In recent years, significant progress has been seen in robot-assisted surgery and computer-assisted surgery. The segmentation of surgical instruments can accurately locate robotic instruments and estimate their posture, which is essential for the navigation of surgical robots. In addition, the segmentation results can be used to predict dangerous operations and reduce surgical risks. At the same time, it can provide a variety of automated

solutions for postoperative work, such as objective skill evaluation, surgical report generation, and surgical process optimization, which are of great significance to clinical work.

Model

The method in this paper integrates three models for fusion, namely Polyp-PVT, Sinv2-PVT, and Transfuse-PVT. The official Polyp-PVT [[dong2021PolypPVT](#)] is designed for polyp segmentation and achieves SOTA segmentation capabilities and generalization performance. It uses transformer as the backbone network to extract richer features and solves the impact of colorectal image acquisition. Here, we adopt the standard structure without any modification. For the Transfuse [[zhang2021transfuse](#)], which is also adopted in the polyp segmentation, we improve it by replacing the transformer part with the PVT [[wang2021pyramid](#), [wang2021pvtv2](#)] to enhance its performance. The official Sinv2 [[fan2021concealed](#)] proposes an end-to-end network for search and recognition the concealed Object, which obtains considerable segmentation performance. This task is similar to the polyp segmentation and surgical instrument segmentation, so we adopt. Here we employ a stronger PVT transformer [[wang2021pyramid](#), [wang2021pvtv2](#)] to replace the original res2net [[gao2019res2net](#)] backbone to extract more powerful features.

Hyperparameter settings

We use the PyTorch framework to implement our model, and use Tesla V100 to accelerate the calculation. Taking into account the difference in the size of each polyp image, we adopted a multi-scale strategy in the training phase. The hyperparameter details are as follows. To update the network parameters, we use the AdamW optimizer, which is widely used in transformer networks. The learning rate is set to 1e-4, and the weight attenuation is also

arXiv:2108.06932v8 [eess.IV] 19 Feb 2024

Table 1: 5-fold cross-validation results of surgical instrument segmentation. Intersection-Over-Union (Jaccard index), Dice coefficient, and the pixel accuracy are abbreviated as IoU, Dice, PA respectively.

models	Metrics	Flod-1	Flod-2	Flod-3	Flod-4	Flod-5	Mean
Polyp-PVT	IoU	0.9012	0.8744	0.9310	0.9529	0.9522	0.9224
	Dice	0.9427	0.9226	0.9616	0.9754	0.9748	0.9554
	PA	0.9915	0.9900	0.9939	0.9937	0.9934	0.9925
Sinv2-PVT	IoU	0.8971	0.8760	0.9315	0.9521	0.9519	0.9217
	Dice	0.9392	0.9237	0.9622	0.9751	0.9745	0.9549
	PA	0.9908	0.9897	0.9940	0.9936	0.9934	0.9923
Transfuse-PVT	IoU	0.9034	0.8691	0.9313	0.9497	0.9511	0.9209
	Dice	0.9443	0.9207	0.9611	0.9734	0.9742	0.9547
	PA	0.9917	0.9891	0.9931	0.9925	0.9930	0.9919

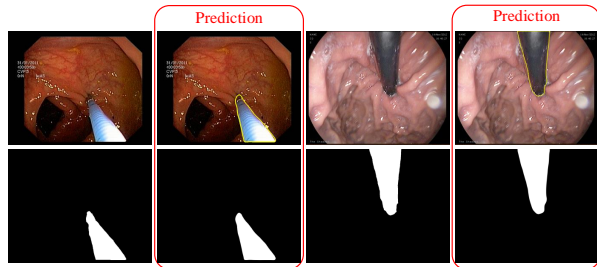


Figure 1: Qualitative description of our prediction.

adjusted to $1e-4$. In addition, we adjusted the size of the input image to 352×352 , the mini-batch size was 16, and it lasted 100 epochs. The total training time is close to 4 hours to achieve the best (for example, 40 epochs) performance. For testing, we only adjust the image size to 352×352 without any post-processing optimization strategy. It is worth noting that all three models use the same hyperparameter settings.

Training stage:

We use the same training strategy to train Polyp-PVT, Sinv2-PVT, and Transfuse-PVT. Specifically, we first divide the dataset into 5 groups (folds). At each time, we use 4 groups of dataset as the training set and the remaining one as the validation set. During training, we keep the model weights with the best IoU on the validation set. After 5-fold training, all of Polyp-PVT, Sinv2-PVT, and Transfuse-PVT have 5 model weights, and a total of 15 different model weights are obtained.

Inference stage

In the inference stage, for the input images, we only resize the images to 352×352 without any data enhancement. For the output, we upsample it to the original feature size. So, we can obtain 15 different prediction results of test dataset without any data enhancement.

In order to obtain a more stable prediction, we merge the 15 prediction results with a minority voting method. Because the voting strategy will produce many

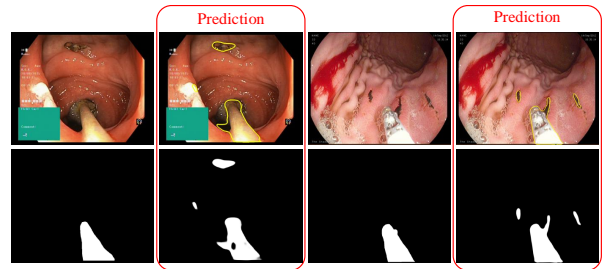


Figure 2: Some failure cases in surgical instrument segmentation

independent noise pixels on the edge of polyps or surgical instruments. We use open operation and counting to remove. First, the open operation is used to remove independent noise points, and then the area of the block in the prediction image is counted to remove relatively small noise blocks in the prediction image, so as to obtain the final prediction result.

Result

We show the qualitative results in Fig. 1, and give the results of the evaluations in Tab. 1. At the same time, we shared our failure cases in Fig. 2.

Discussion

It can be found that both of our improved algorithms Sinv2-PVT and Transfuse-PVT have the same performance as polyp-pvt. In the 5-fold cross-validation, the three results are relatively stable. There are results above 0.92 on the IoU, and we give some visual results in 1.

However, there are certain shortcomings shown in 2. Our results almost correctly segment the equipment, but introduce some noise. One characteristic of these noises is that they are biased towards black. This is mainly due to the fact that there are more black instruments in the entire data set. Therefore, small black areas (food residuals, etc.) in the colonoscope will be identified as surgical instruments. These noises can be filtered by the

size of the area to achieve the purpose of noise removal.

Conclusion

In this paper, we propose a robust generalized medical image segmentation framework, which is composed of multiple models, and uses the pyramid vision transformer backbone as an encoder to explicitly extract more powerful and powerful features.

Acknowledgments

I would first like to thank the researcher Dengping Fan in IIAI, whose expertise was invaluable in formulating the research questions and methodology.

Conflict of interest

Authors state no conflict of interest. (Either keep this sentence or describe any conflict of interest.)